Probing electron transfer processes in Y PO_4:Ce, Sm by combined synchrotron–laser excitation spectroscopy

2010 J. Phys.: Condens. Matter 22 185403

(http://iopscience.iop.org/0953-8984/22/18/185403)

J. Phys.: Condens. Matter **22** (2010) 185403 (12pp) doi:10.1088/0953-8984/22/18/185403

Probing electron transfer processes in YPO_4:Ce, Sm by combined synchrotron–laser excitation spectroscopy

N R J Poolton[1,2], A J J Bos[3], G O Jones[2] and P Dorenbos[3]

[1] Photon Science Institute, Manchester University, Oxford Road, Manchester M13 9PL, UK
[2] Institute of Mathematics and Physics, Aberystwyth University, Aberystwyth SY23 3BZ, UK
[3] Faculty of Applied Sciences, Delft University of Technology, Delft, Mekelweg 15, 2629 JB Delft, The Netherlands

Received 3 March 2010, in final form 27 March 2010
Published 15 April 2010
Online at stacks.iop.org/JPhysCM/22/185403

Abstract

Yttrium phosphate co-doped with cerium and samarium acts as a charge storage phosphor, but in highly doped material (0.5% co-doping levels), the proximity of defects leads to the uncontrolled non-radiative loss of stored charge through tunnelling. In order to characterize these defects, their mutual interactions and intra-pair charge transfer routes, experiments have been undertaken in which a laser probe is deployed during luminescence excitation using a synchrotron. Two modes of operation are described; in each case, the laser (2.8 eV) probes only Sm^{2+} ions, and the detection is set to monitor exclusively Ce^{3+} 5d–4f emission. Mode 1: the sample is pumped with monochromatic synchrotron photons in the range 4.5–12 eV, and the resultant charge populations probed with the laser 30 s later; this has the effect of sampling electrons trapped at Sm^{2+} that are in quasi-equilibrium. Here, a clear transition between a sub-bandgap Urbach tail region and excitations above the mobility edge is especially apparent, enabling an accurate value of the conduction band energy of YPO_4 to be determined, 9.20 eV. Furthermore, the Sm^{2+} and Ce^{3+} ground state energies can be positioned within the bandgap (6.8 eV and 3.85 eV above the top of the valence band, respectively). Mode 2: the sample is pumped with monochromatic synchrotron photons in the range 4.5–12 eV and, during this pumping process, the laser probe is activated. This more dynamic process probes direct electron transfer excitation processes between spatially correlated Sm–Ce defect pairs, via their excited states; the laser probe enhances the Ce^{3+} emission if direct electron transfer from the Ce^{3+} ground state to the excited states of Sm^{2+} is being pumped, or quenches the luminescence if the Ce^{3+} excited states are pumped. The experiments allow for a precise measure of the difference in energy between the Sm^{2+} and Ce^{3+} ground states (2.98 eV).

(Some figures in this article are in colour only in the electronic version)

1. Introduction

Doping wide bandgap materials with divalent or trivalent lanthanide ions has the effect of introducing defects that can be used for a wide variety of applications such as display phosphors and persistent luminescent materials (e.g. aluminates doped with Dy^{2+}, Eu^{3+}; Dorenbos 2005a), charge storage phosphors for use in luminescence dosimetry applications (e.g. Lakshmanan 1999), scintillators and many more. The research area has been greatly enhanced recently by the introduction of a model (Dorenbos 2003, Dorenbos *et al* 2010) which enables a prediction to be made concerning the energy levels of the whole lanthanide series in a particular material, provided that the energy of just one defect is known.

Recently, systematic studies of the trap depths of the $[Nd, Sm, Dy, Ho, Er, Tm]^{3+}$ series in the wide-gap material YPO_4 (co-doped with Ce) has confirmed the accuracy of the model (Bos *et al* 2008, Dorenbos and Bos 2008). During these studies however, the system co-doped with both Ce and Sm showed anomalous results in that, although both charge-carrier trapping defects were determined to be very deep lying below the conduction band edge (making the charge thermally stable

at room temperature), a strong prevalence was found for non-thermal charge loss from the defects, which was interpreted as arising from non-radiative intra-pair electron tunnelling following irradiation of the samples.

Knowledge of non-thermal tunnelling processes of charge carriers between spatially correlated defects has relevance to a number of disciplines, including radiation dosimetry measurements; in geological dating of silicate-based sediments for example, the charge loss from thermally stable charge trapping centres can yield underestimation of accumulated dose and hence calculated age (e.g. Huntley and Lamothe 2001). Whilst their effects can thus be profound, providing information on the detailed mechanisms of such tunnelling processes cannot easily be established by simple irradiation/read-out measurements alone (e.g. via thermoluminescence). However, recent work at Daresbury synchrotron (Poolton *et al* 2005, 2006) has shown that the simultaneous use of both monochromatic x-rays (to populate charge trapping centres) and laser (to de-populate them) in both pump-and-probe and pump-then-probe modes can provide a route to better understanding of the dynamics of charge transfer processes in wide bandgap materials that specifically involve the mediation of defect states. In this paper, we describe the results of such experiments when applied to the fading YPO_4:Ce, Sm system for synchrotron-based measurements in the trans-bandgap energy range 4–12 eV. This material system is a particularly useful one, not only because of the rapidity of the known tunnelling charge loss, but because the Ce and Sm only form single trapping defects in the simple lattice structure (Dorenbos and Bos 2008). The choice of the (Ce, Sm) co-doped system has added value since the ion pair is often used in photostimulated luminescence materials in which the Sm acts as an electron trapping centre, and Ce the luminescence centre: examples are MgS:Ce, Sm (Mathur *et al* 1986), CaS:Ce, Sm (Chakrabarti *et al* 1989), SrS:Ce, Sm (Keller and Pettit 1958), Y_2SiO_5:Ce, Sm (Meijerink *et al* 1991) and $LiLnSi_4$:Ce, Sm (Sidorenko *et al* 2006).

The results of this work on YPO_4 provides valuable data on the precise location of the Ce^{3+} and Sm^{2+} ground state energy with respect to the valence and conduction band, and with respect to each other. Evidence will be provided for an optically excited electron transfer from Ce^{3+} directly to Sm^{3+} without the involvement of conduction band states.

2. Experimental details

Powdered samples of yttrium phosphate were synthesized by solid state reaction, with both Ce and Sm concentrations set at either 0.5% or 0.1% (referred to hereafter as the 'high' and 'low' doped materials, respectively); the purity of the resulting sample phase was checked by x-ray diffraction.

Synchrotron-based luminescence experiments were undertaken on beamline 3.2 (4–40 eV) at Daresbury synchrotron radiation source (SRS) in the UK. The Mobile Optical Luminescence End Station, MOLES (Quinn *et al* 2003) was used throughout for all measurements; unless otherwise stated, these were carried out at 10 K, and spectra have been corrected for energy-dependent instrumental responses.

In the case of both optically stimulated luminescence (OSL) and combined synchrotron/laser excitation spectroscopy, the detection window is fixed using 6 mm of Schott UG11 filters in front of a bialkali (UV-green sensitive) photomultiplier tube; these filters provide a detection window in the energy range 3.26–4.13 eV, which exclusively samples the Ce^{3+} 5d–4f emission from the sample. Note that this detection window is chosen to be on the high photon energy side of the lasers used, but on the low photon energy side of the synchrotron light: this ensures that either the de-trapping OSL signal, or laser-induced changes to any synchrotron-pumped signal are monitored; it specifically discriminates against any steady-state luminescence that could be excited by application of the laser alone.

For slowly time-varying laser-induced signals ($t > 1\ \mu$s), a modulating 445 nm diode laser module was used in conjunction with (but not synchronized to) the synchrotron when acting in quasi-CW mode (i.e. for experimental timescales much longer than the inherent pulsed structure of synchrotron light). This 40 mW laser, with modulation rates from CW to 20 MHz, provided $\sim$250 mW cm^{-2} at the sample over an area of $\sim$16 mm^2, which is sufficient to cover the synchrotron beam footprint of $\sim$0.5 $\times$ 1.5 mm. The synchrotron light was activated/deactivated by means of a mechanical shutter (beam switching speed, $\sim$10 ms).

3. Results and discussion

3.1. Luminescence excitation and emission spectra

Before considering the more complex issue of charge (in our case electron) transfer processes between defect energy states, it is fruitful to put the measurements in context by considering the basic luminescence excitation and emission processes active in YPO_4:Ce, Sm. It should be noted that the lowest energy equilibrium configuration of the defect charge states is Sm^{3+} and Ce^{3+}.

For above bandgap excitation, strong luminescence is observed resulting from the well documented internal 5d–4f transitions of Ce^{3+} and internal 4f–4f transitions of Sm^{3+} ions, occurring in the UV (3–4 eV) and red (1.5–2.2 eV) spectral regions, respectively. For comparative previous studies of these emissions in this material, see e.g. van Pieterson *et al* (2002), Bos *et al* (2008), Karanjikar and Naik (1988), Krumpel *et al* (2009). For selective sub-bandgap excitation, these emission bands are displayed in figure 1(a) (5.0 eV and 7.1 eV excitation for Ce^{3+} and Sm^{3+}, respectively). The full excitation spectra of these emission bands can be easily obtained by scanning the synchrotron energies, as shown in figure 1(a) in the spectral range 4.5–12 eV; all of the well defined spectral features in the range 4.5–7.8 eV result from 4f–5d excitation of the Ce^{3+} and Sm^{3+} ions, allowing an accurate measure of the excited state level energies with respect to their ground state; these spectra are almost identical with those measured by van Pieterson *et al* (2002), whose detailed work allows the transitions to be identified. In the case of Ce^{3+}, we observe a set of sharp excitation peaks at 5.00, 5.22 and 5.51 eV (labelled B, C and D respectively by van Pieterson, representing excitation to the

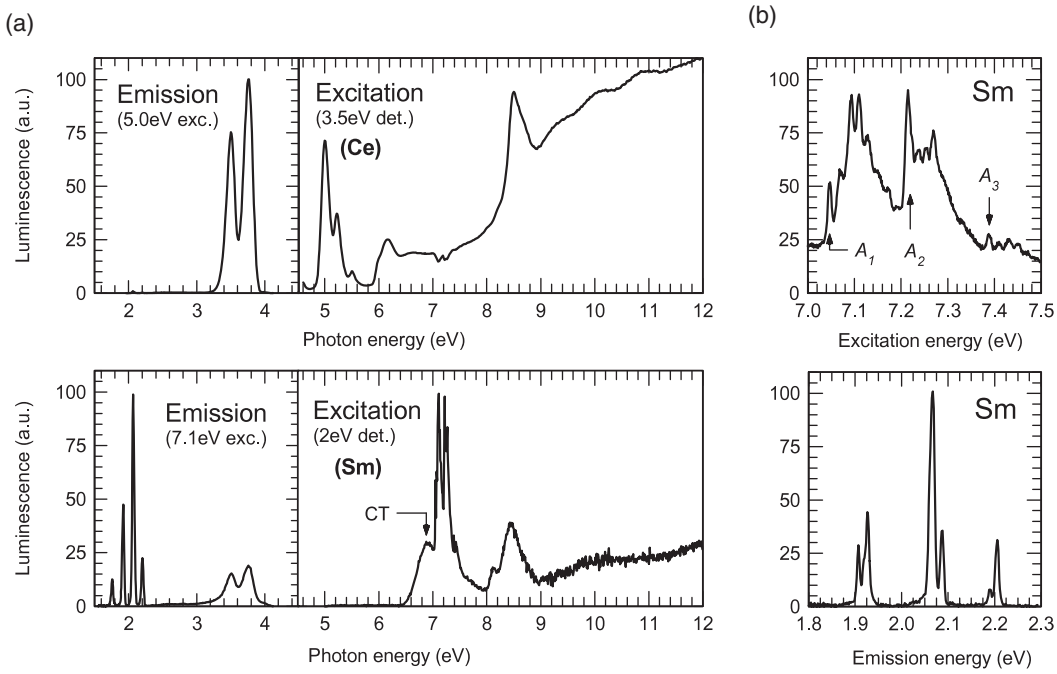

Figure 1. (a) Luminescence excitation and emission spectra of Ce^{3+} and Sm^{3+} in co-doped YPO_4:Ce, Sm (shown for 0.5%, 'high' doped sample; the low-doped material is similar). 'CT' refers to the charge transfer band. (b) Details of the more finely structured Sm^{3+} excitation and emission spectra (above and below, respectively). $A_{1,2,3}$ depict the fine structure of the excited $5d_1$ states of Sm^{3+}.

$5d_2$, $5d_3$, $5d_4$ levels) together with a broader peak at 6.16 eV, having a prominent shoulder at 5.98 eV (both features coming under van Pieterson's 'E-band' descriptor for $5d_5$). A common feature at 8.5 eV occurs in both the Sm^{3+} and Ce^{3+} excitation spectra, and is attributed to exciton creation in the YPO_4 host lattice. For the Sm^{3+}, a broad band at ∼6.9 eV is also observed, which is ascribed to the charge transfer band, and as such is labelled 'CT'. Figure 1(b) shows the more detailed excitation and emission spectra of Sm^{3+} ion to be examined; the sharp features in the excitation range 7.0–7.5 eV show both fine structure splitting of transitions to the lowest 5d level (labelled A_1, A_2 and A_3 by van Pieterson *et al* (2002), and measured at 7.0487 eV, 7.215 eV, 7.388 eV respectively in our experiment), together with their associated phonon replicas. Because of the high doping levels, these Sm^{3+} A-bands can be observed as dips in the Ce^{3+} excitation spectra, due to the Sm absorption.

The excitation spectra of the Ce^{3+} and Sm^{3+} ions shown in figure 1 provide much information on the excited states of the individual ions; furthermore the energy of the CT band of Sm^{3+} provides us with the location of the Sm^{2+} ground state above the top of the valence band. The exciton band E^{ex} at 8.5 eV can also provide us with an estimate for the optical bandgap of YPO_4; as a rule of thumb the exciton binding energy is about 8% of the exciton creation energy (e.g. see Dorenbos (2005b)), thus we estimate 9.2 eV for the high mobility bandgap E_{VC}. There is, however, no information from figure 1 regarding interactions between the defects (including any non-radiative transition processes); the following sections show how the additional use of a laser probe in the experiments can provide a wealth of additional (and/or more accurate) information on the positions of the defect levels, their mutual interactions and bandgap energy, depending on how the laser and synchrotron stimulations are deployed.

3.2. OSL, photo-transferred OSL and the energy level scheme

The simplest application of both synchrotron and laser excitation is depicted in figure 2, whereby the sample is excited for a period by the synchrotron (during which steady-state luminescence is observed), followed by some delay period before applying a laser pulse. For above bandgap synchrotron stimulation, free electron–hole pairs are created that can be captured by the Sm and Ce ions respectively, changing their charge state:

$$Ce^{3+} + h \rightarrow Ce^{4+} \quad (1)$$

$$Sm^{3+} + e \rightarrow Sm^{2+}. \quad (2)$$

The resulting charge states of the ions are sufficiently deep below the conduction band so as to be time-stable, unless tunnelling processes between them allow the conversion back to their original charge states (Dorenbos and Bos 2008). However, the application of the laser allows the release of electrons from the Sm^{2+} to the conduction band, wherein it is free to recombine with the Ce^{4+}, in the process

$$Sm^{2+} + h\nu(\text{laser}) \rightarrow Sm^{3+} + e(CB) \quad (3)$$

$$Ce^{4+} + e(CB) \rightarrow (Ce^{3+})^* \rightarrow Ce^{3+} + h\nu(\text{OSL}). \quad (4)$$

Here, the '*' signifies an excited state of the ion. This is very simply a photon write–read (or charge dosimetry) process, where synchrotron light is used to charge the ions, and the laser discharges them producing 'optically stimulated luminescence' (OSL), which decays with time as the charge

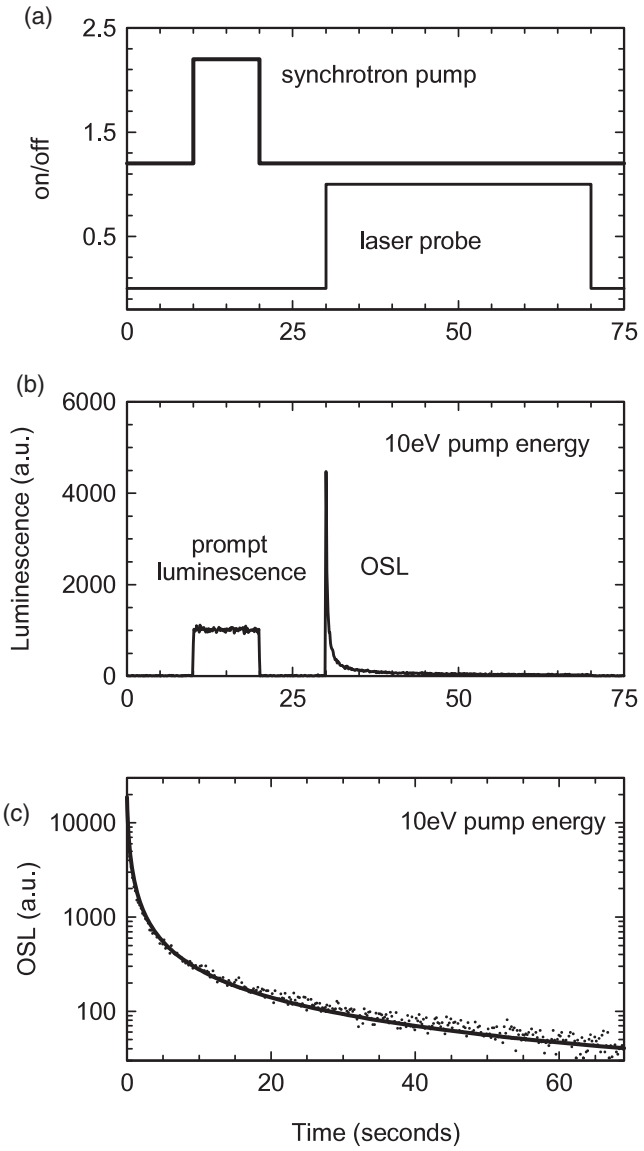

Figure 2. (a) Schematic of the pulse sequence of the synchrotron and laser in the experiments designed to first induce ions in the charge states Sm^{2+} and Ce^{4+}, then probe transfer of charge between them to convert them back to Sm^{3+} and Ce^{3+}. The experiment is designed such that the laser probes Sm^{2+} and Ce^{4+} that are in quasi-equilibrium. (b) The resulting luminescence yield, when the internal UV emission of Ce^{3+} is monitored during the sequence given above. The synchrotron itself induces steady-state luminescence (at this energy, 10 eV), and the laser stimulates time-decaying optically stimulated luminescence (OSL) due to the transfer of charge from one defect to another. (c) The OSL decay (on a logarithmic scale) is shown to follow the general order kinetics of equation (5) (data shown as points; fitted data shown as the solid line).

conversions take place, and whose emission characteristics are expected to be exactly that of the Ce^{3+} ion as depicted in figure 1. The time-decay process of the OSL after 10 eV synchrotron pumping is shown in figure 2(c) to be that of general order kinetics, and follows the form (over three orders of magnitude intensity change):

$$I_{\mathrm{OSL}}(t) \propto \frac{1}{(1+\lambda t)^{\alpha}}. \qquad (5)$$

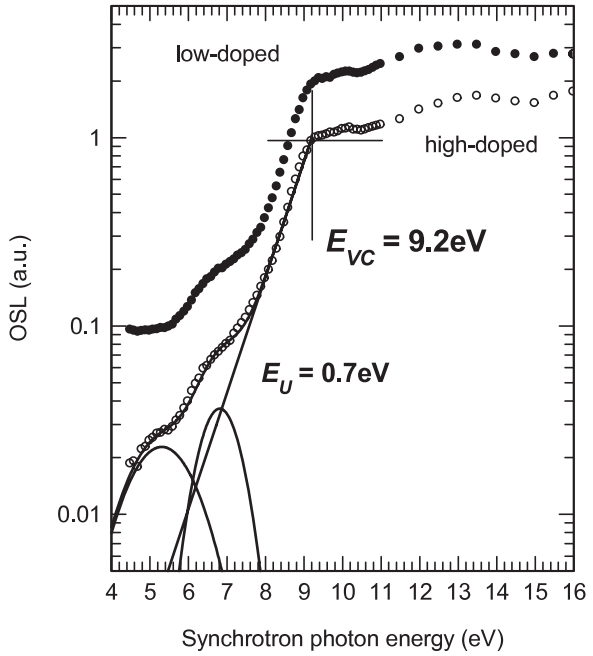

Figure 3. Intensity of the OSL signal (as induced during the sequence of figure 2(a)) as a function of the synchrotron pump photon energy, for both high- and low-doped materials. The bandgap E_{VC} is clearly depicted as the transition between the supra- and sub-bandgap excitation regimes. The exponential Urbach tail is clearly depicted (with the Urbach tail extent E_{U} given), together with resonances at lower energy fitted here using Gaussians.

A fitting provides $\lambda = 6.63\ \mathrm{s}^{-1}$ and $\alpha = 1.0$ (dimensionless). The key point about these experiments, however, is that the laser can probe the presence of Sm^{2+} no matter how the original $Sm^{3+} \rightarrow Sm^{2+}$ charge conversion has been achieved, and this can involve sub-bandgap processes, as well as direct ionization of the lattice. The energy-resolved dependence of photo-transfer into the OSL active ion centres (PT-OSL) is thus potentially a valuable source of information as to the various transfer processes active.

Figure 3 shows the energy-resolved photon excited electron transfer into the Sm OSL centres for both the high- and low-doped YPO_4:Ce, Sm samples. Unlike the highly complex luminescence excitation spectra displayed in figure 1, the spectrum is much simpler to understand and essentially displays three separate features: (i) for above bandgap excitation (10–16 eV), the resulting OSL changes very little in intensity with photo-excitation energy. (ii) Sub-bandgap stimulation induces an exponentially variable intensity change. (iii) In the sub-bandgap regime (and superimposed on the exponential tail) two weak resonant processes are identified, peaking at 5.3 and 6.8 eV.

Although simple in its execution, this experiment yields three important parameters. Firstly, the exponentially variable process clearly depicts the sample's Urbach tail, and the transition energy from Urbach excitation to excitation above the mobility edge E_{VC} is well defined, allowing an accurate measure of the latter to be realized: we determine this to be (9.20 ± 0.05) eV at 10 K from the curve; this is in excellent agreement with our rule of thumb $E_{\mathrm{VC}} = 1.08E^{\mathrm{ex}}$

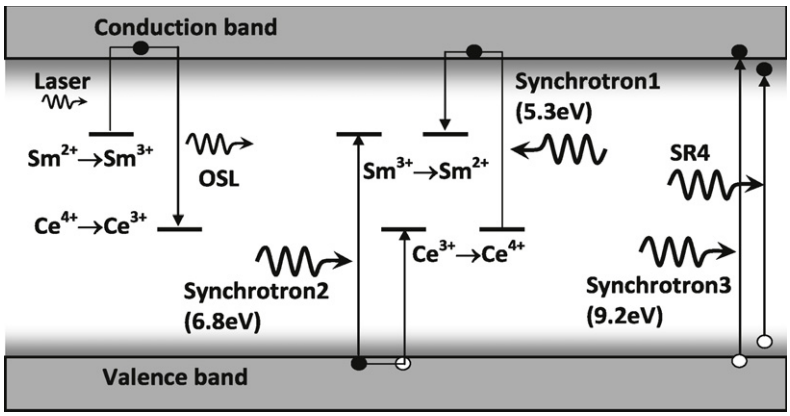

Figure 4. Schematic energy level scheme for YPO_4:Ce, Sm as derived from the results of figure 3. On the left of the diagram, the mechanism of laser-induced OSL emission is depicted, and on the right, the mechanisms by which the synchrotron pump can induce the defect charge states that can be probed by the laser. These are depicted as synchrotron 1, 2, 3, 4, and correspond (respectively) to direct interactions with the Sm and Ce defects, band-to-band excitation (via the high mobility states) and band-to-band excitations (via the Urbach tails).

mentioned in section 3.1. The Urbach energy E_U is also determined to be 0.7 eV; this is a useful value since it can inform us of any excited states of the defects that may be located within the tails. Finally, the position of the resonances are also important; recalling that the experiment identifies *only* transfer processes that create Sm^{2+}/Ce^{4+} charge states (which the OSL process reverses), it is inferred that these sub-bandgap resonances induce processes that involve direct electronic transitions involving the defects both to and from the valence/conduction bands, namely:

$$[Sm^{3+}, Ce^{3+}] + h\nu(6.8\ \text{eV}) \rightarrow Sm^{2+} + \text{h(VB)} + Ce^{3+} \rightarrow [Sm^{2+}, Ce^{4+}] \quad (6)$$

$$[Sm^{3+}, Ce^{3+}] + h\nu(5.3\ \text{eV}) \rightarrow Ce^{4+} + \text{e(CB)} + Sm^{3+} \rightarrow [Sm^{2+}, Ce^{4+}]. \quad (7)$$

Crucially, if the assignment of the two resonances in figure 3 to the process depicted in equations (6) and (7) is correct, the experiment allows the accurate positioning of the energy levels within the bandgap. Equation (6) expresses the VB electron transfer to Sm^{3+} with subsequent capture of the valence band hole by Ce^{3+}; the 6.8 eV band in figure 3 is also observed as the 6.9 eV Sm CT band in figure 1(a). More uniquely, equation (7) expresses that the Ce^{3+} defect lies 5.3 eV below the conduction band, and this information is not available from the simple luminescence excitation spectra alone. Further confirmation of the assignments is given in sections 3.3 and 3.4.

Figure 4 is used to summarize all the charge conversion processes discussed in this section, including the basic OSL process which is used to probe them. As the measurements probe only the ground state of the defects in their respective charge states, these are shown as such, without the added complexity of their excited states: the latter are shown to become rather more important in the following section. The energy level scheme suggests that the difference in energy between the Ce^{3+} and Sm^{2+} defect levels is 2.9 eV (i.e. $[6.8\ \text{eV} - (9.2 - 5.3\ \text{eV})]$), and this is a crucial parameter if interactions between the defects are to be considered; in the following section, this energy separation is measured much more precisely (to be 2.98 eV) via photon energy-resolved excitation of electron transfer from Ce to Sm, and will confirm the basic model interpretation presented here.

3.3. Prompt synchrotron-plus-laser excitations

3.3.1. General overview. The experiments described in section 3.2 probe inherently slow processes; they monitor defects that retain their charge states (at least over the course of the measurement, i.e. minutes) and are thus a monitor of the quasi-equilibrium $[Sm^{2+}, Ce^{4+}]$ population. If more dynamical interactions between the defects are to be probed, the experiment can be modified by bringing the laser-activation window *within* that of the synchrotron pulse, as shown schematically in figure 5(a). The timing sequences are long enough that the synchrotron can still be considered as acting in a quasi-CW mode, with synchrotron light being activated and deactivated by means of a mechanical shutter. In order to ensure that there is no residual population of $[Ce^{4+}, Sm^{2+}]$ (i.e. all ions are in the charge state $[Ce^{3+}, Sm^{3+}]$), prior to the timing sequence of figure 5(a), the laser is applied for 30 s.

Activating a laser pulse during the synchrotron irradiation can have a number of different effects, depending on the synchrotron photon energy. For example, with above bandgap synchrotron irradiation ($E > 9.2$ eV), the laser can induce a CW intensity change in the resultant luminescence yield (Δ_1), as demonstrated in figure 5(b); deactivation of the laser probe typically sees the luminescence return to the synchrotron-only emission intensity very quickly (<10 ms, the timing resolution of this particular experiment). If the laser is applied after the synchrotron has been active for a period, some conversion from $[Sm^{3+}, Ce^{3+}]$ to $[Sm^{2+}, Ce^{4+}]$ may have taken place via electron and hole capture (processes by equations (1) and (2)) and this is reversed on application of the laser, producing a burst of OSL light, the dynamics of which are always found to be identical to the OSL described in section 3.2.

During above bandgap excitation, the resulting luminescence yield is an equilibrium between direct recombination of charge at the Ce sites (process governed by equation (4)) and charge trapping at the Sm sites (process governed by

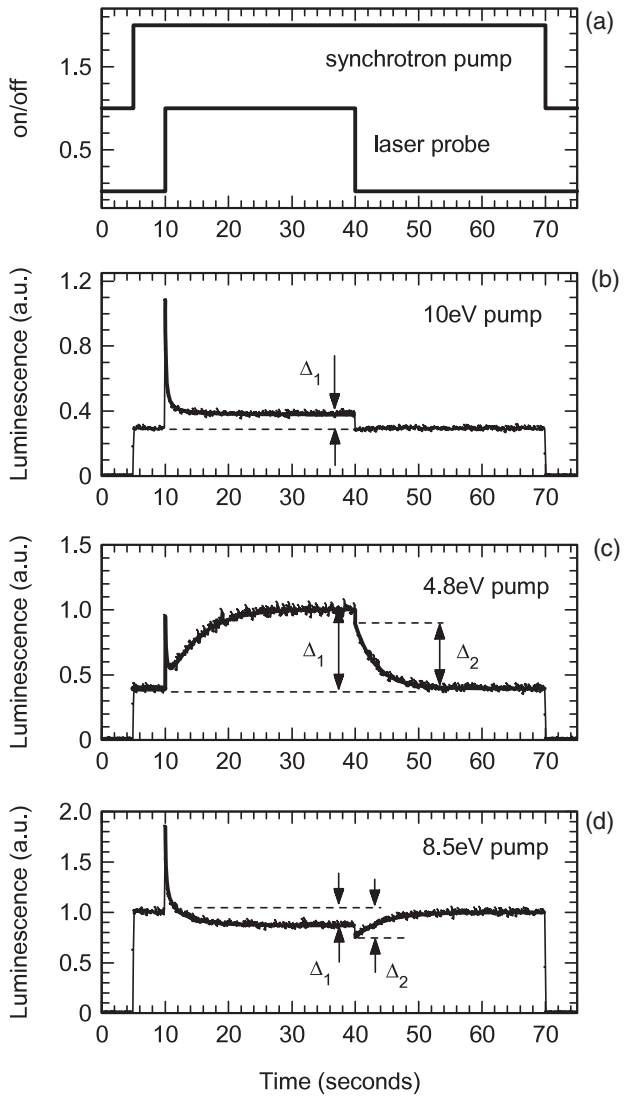

Figure 5. (a) If the quasi-equilibrium experiment depicted in figure 2 is modified such that the laser probe pulse is activated during the synchrotron pump pulse, then more dynamical processes can be analysed. These depend strongly on the pump energy used, shown here for three examples at 10 eV, 4.8 eV and 8.5 eV in (b), (c), (d) respectively. The origin of the energy-dependent luminescence yield changes Δ_1 and Δ_2 are discussed in the text.

equation (2)); the CW application of the laser during this excitation process simply changes this equilibrium condition by immediately evicting electrons from the Sm^{2+} sites, increasing the Ce^{3+} emission yield, Δ_1. For sub-bandgap synchrotron excitation however, much more complex and dynamic processes are observed when the laser is activated and deactivated, and these are highly dependent on the precise synchrotron photon energy. Examples of this are given in figures 5(c) and (d) for excitation at 4.8 eV just below the second 5d band of Ce^{3+} and excitation at 8.5 eV in the exciton band. At 4.8 eV, for example, the luminescence does increase on application of the laser, but the rise is slow (a saturating exponential; $\tau = 5$ s for this energy). Thus, Δ_1 is taken as the equilibrium intensity in the saturation part of the exponential term. Whilst the synchrotron is still active, but the laser is deactivated, two things typically happen; there is first a very rapid intensity change (timescales <10 ms) followed by a slow exponential decay in the luminescence intensity back to the equilibrium synchrotron-only luminescence yield; the intensity of this latter component is labelled Δ_2 in the figure. In contrast, at other synchrotron pump energies, laser activation can lead to *quenching* of the synchrotron-only luminescence yield (so Δ_1 here is negative, rather than positive); an example is given in figure 5(d) for 8.5 eV excitation. In such circumstances, removal of the laser whilst the synchrotron is still active yields a *further* quenching of the luminescence (timescale <10 ms) followed by a slow increase back to the equilibrium synchrotron-only luminescence yield; so here Δ_2 is also negative.

3.3.2. Interpretation of the signals I: transition energies. The meaning of these complex transients cannot readily be explained in isolation, but by undertaking the measurements across the full excitation range 4.5–16 eV, and comparing the results of both the high- and low-doped samples, their meaning starts to emerge. In figure 6, the transient level changes Δ_1, Δ_2 and the difference $(\Delta_1 - \Delta_2)$ are plotted as a function of the synchrotron pump energy for the high-doped sample. The first and most easily defined feature of figure 6 is that of the fast-response level difference $(\Delta_1 - \Delta_2)$; this follows exactly the form of the PT-OSL shown in figure 3, with the bandgap energy clearly identified as a transition between the Urbach tail region and the above-bandgap transitions, and two weak bands at low energy; each of these features have the same energies as identified in the experiment used for figure 3 (0.7 eV for E_U and 5.3 and 6.8 eV for the weak bands). The integrated intensity of the OSL signal in figure 3 is a measure of the total steady-state number of Sm^{2+} defects created during the synchrotron pump, whilst $(\Delta_1 - \Delta_2)$ is a measure of the change in that steady-state number due to the laser pump. Thus, a more or less proportional relationship as demonstrated by our results is not too surprising. In section 3.3.2 we will argue that spatially non-correlated Ce^{4+} and Sm^{2+} defects are involved in this process. The response is fast because electrons move on a timescale much faster than 10 ms through the conduction band in order to establish the new equilibrium defect concentration.

Apart from the intense transient changes in the exciton absorption region of the spectrum 8.2–8.7 eV (which will be considered separately in section 3.3.4) the most complex synchrotron–laser interactions occur in the excitation range 4.5–7 eV, and these features are shown in more detail in figure 7(a); as both Δ_1 and Δ_2 behave in similar manner, for clarity, Δ_2 is used in the spectral analysis here.

The first point to note from figure 7(a) is that the dominant peaks at 4.88 and 5.90 eV (with a weaker, broader peak at 5.50 eV) do not correspond to anything in the luminescence excitation spectra of figure 1, and it is thus clear the experiment is certainly *not* involving the excitation of either Sm or Ce in isolation. In contrast, the dips in the spectrum (either negative, or tending to negative) at 5.0, 5.2 eV and, continuously from 6 to 8 eV, however, do correspond directly to the peaks in the luminescence excitation spectra of Ce^{3+} (figure 1(a)), and clearly must directly involve excitation of this ion species.

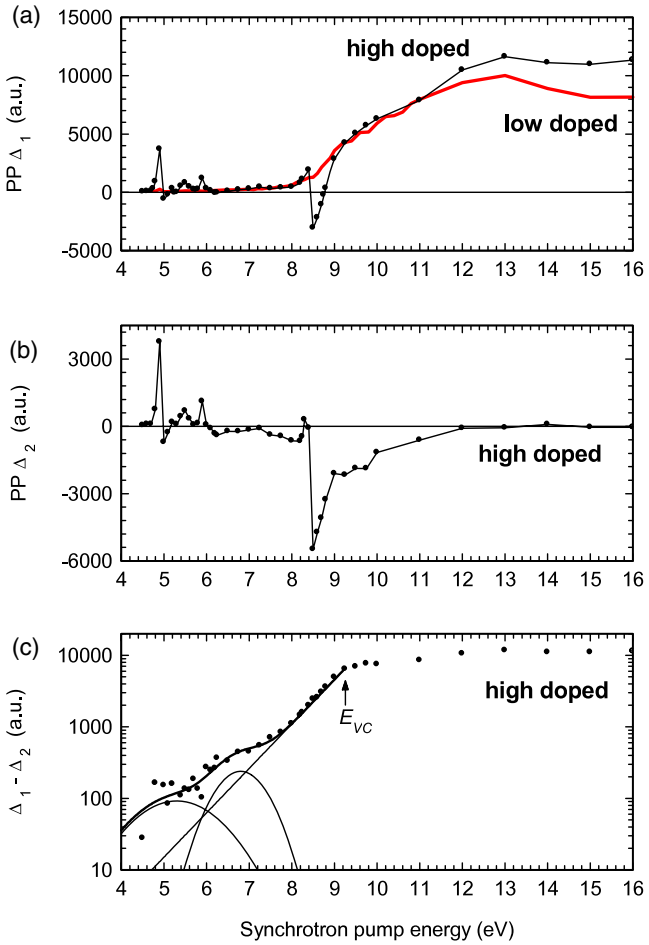

Figure 6. Pump energy dependence of the laser probe induced luminescence changes in luminescence for (a) Δ_1, (b) Δ_2 and (c) $\Delta_1 - \Delta_2$ (see figure 5 for the meaning of Δ_1 and Δ_2); note the log scale. As shown in (a), the biggest signals are induced in the high-doped sample; for the low-doped sample, the signal change is similar to that depicted in figure 3 for the charge in quasi-equilibrium. The sharp spectral features are thus related to interactions between spatially correlated defects. In (c) the data for energy below E_{VC} is fitted to an exponential tail and two Gaussians, each with the same energy parameters as the features of figure 3.

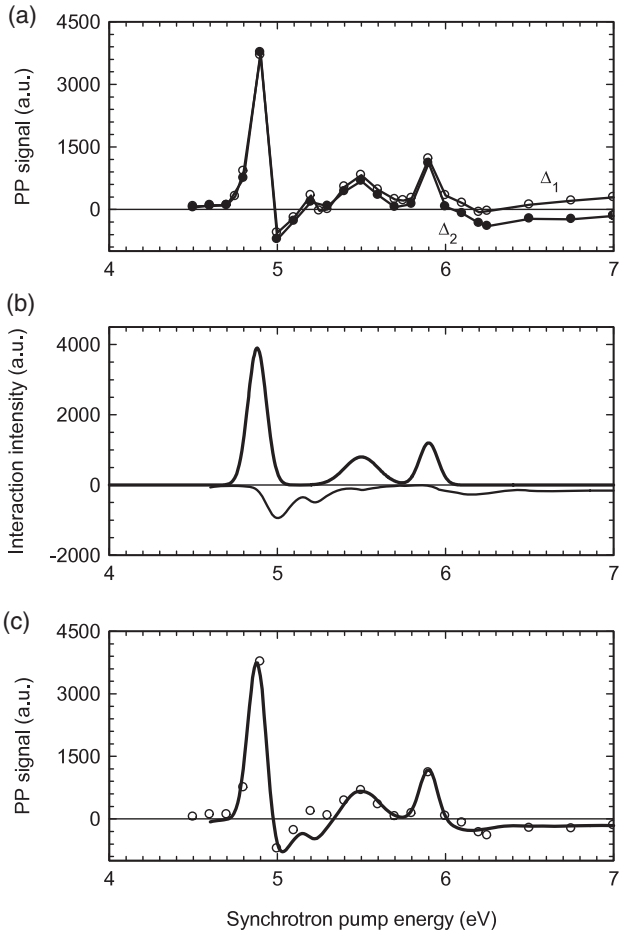

Figure 7. (a) Detail of the low energy pump–probe interaction signals Δ_1 and Δ_2, taken from figure 6. (b) The dips in the PP signal correspond with the Ce^{3+} excitation spectrum (shown in full, inverted, for comparison); the peaks therefore correspond to a new set of signals in the sample, as shown by the positive spectrum made as a first guess. (c) Combining the two curves yields a resultant PP spectrum as shown by the solid line; comparison can be drawn with the experimental data (Δ_2) as shown by the individual points.

Figure 7(b) shows the *inverted* excitation spectra of Ce^{3+} obtained from figure 1, together with a first guess at the positions of the positive peaks in the combined synchrotron–laser excitation spectrum. The combined curves are compared with the experimental data in figure 7(c), where an excellent correspondence is observed.

To understand this combined synchrotron–laser excitation spectrum (figure 7(c)), the key underlying factor is that the laser only has the capability of probing Sm^{2+} ions in this measurement mode, even though an important component of the pump–probe spectrum involves sub-bandgap excitation of Ce^{3+} to its various excited states. Bos *et al* (2010) have recently shown that, rather than using 455 nm (2.79 eV) laser excitation (which excites electrons from Sm^{2+} into the conduction band), energy-resolved OSL stimulation reveals a whole series of 4f–5d excitation bands in the region 1.6–3.0 eV. The relevant spectra at room temperature and at 10 K are shown in figure 8(a), together with the identified $5d_1$, $5d_2$, $5d_3$ excitation bands each comprising of a main band B with a lower energy shoulder band A, correlated with the Sm^{2+} excited 4f and 5d states. Certainly the $5d_1$ level lies below the conduction band edge, so the presence of a resonant OSL excitation signal at 10 K is suggestive of direct excitation from the Sm to Ce, via their excited states (rather than through the conduction band, after thermal excitation from the $5d_1$ level). If the 4f orbitals of Ce^{3+} show some spatial overlap with the excited state orbitals of Sm^{2+} it should be possible to induce the reverse process, whereby electrons are excited from the ground state of Ce^{3+} into the (overlapping) excited states of Sm^{2+}. Clearly this will only occur when Ce and Sm are close neighbours. It is this process that we believe is being induced by the synchrotron pump to yield the positive peaks in the pump–probe spectrum of figure 7(b). Strong confirmation of this concept is provided if the OSL stimulation spectrum and the enhancing pump–probe signals are directly compared, as shown in figure 8(b). Here, the OSL stimulation spectrum

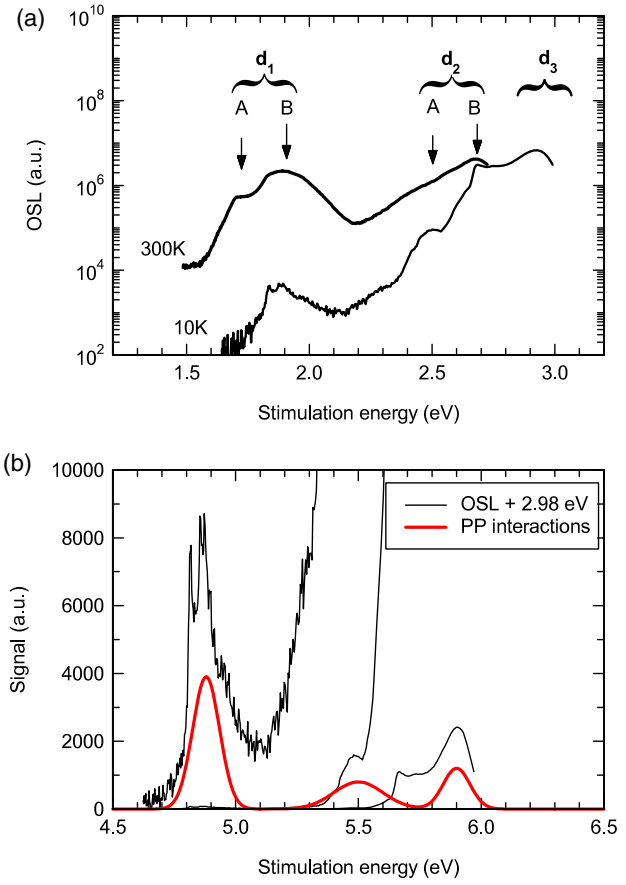

Figure 8. (a) Energy-resolved OSL stimulation spectrum of Sm^{2+} at 300 and 10 K, (see Bos *et al* (2010) for full details). (b) Comparison of the positive-signal PP spectrum component, compared with the Sm^{2+} OSL stimulation spectrum, when shifted by 2.98 eV to higher energy. The correspondence of the peaks indicates that the excited states of Sm^{2+} are active in both spectra, but where the PP signals are derived from excitation from the ground state of Ce^{3+}. The energy shift between the two thus precisely measures the relative energy spacing between the two defects within the bandgap.

is shifted by 2.98 eV to higher energy in order to enable the direct comparison; figure 8(b) shows a direct correspondence with positions of the $5d_1$, $5d_2$ and $5d_3$ resonances in the two cases, though the coarseness of the pump–probe signals do not allow resolution of the A- and B-bands in each of these 5d state resonances. The 2.98 eV energy shift is an important number, as it provides an accurate measure of the difference in ground state energy of the Ce^{3+} compared with Sm^{2+} (i.e. the former lies 2.98 eV below the latter: note that this directly confirms the interpretation of the simple pump-then-probe signals analysed/interpreted in figures 3 and 4). The *intensity* profiles of the OSL and pump–probe resonances are, however, very different. In OSL, electrons excited to the first 5d state of Sm^{2+} would tend to rapidly relax back to the ground state and the electron transfer rate to Ce will be weak at low temperatures. (The OSL signal for this band is strongly thermally dependent, as the process becomes more efficient if electrons can be promoted from the excited state to the conduction band.) After excitation to the higher energy $5d_2$ and $5d_3$ levels the electron has much larger transfer rate to Ce and the OSL signal correspondingly increases. The $5d_3$ level is in the conduction band anyway, from where the electrons are most easily able to move to Ce^{4+} with the resulting OSL emission. In contrast, excitation from the Ce^{3+} ground state to the Sm^{2+} $5d_1$ level is expected to produce the most pronounced pump–probe signal because those transitions are most likely to generate Sm^{2+} (rather than being lost to elsewhere in the lattice if excitation to the higher states is involved). So, in essence the OSL signal increases when higher Sm^{2+} 5d states are excited but the pump–probe signal decreases; their intensities are thus anti-correlated.

Within the model outlined above, data collated from the two-photon experiments thus allow precise positioning and alignment of the Ce^{3+} and Sm^{2+} defects within the energy bandgap, and these are presented in figures 9 and 10. The actual mechanisms of the various pump–probe signals, and their dynamics, are addressed in the following section.

3.3.3. Interpretation of the signals II: laser quenching, enhancement and transition dynamics. In figure 9, the processes behind the laser probe enhancement to the synchrotron pump signal are addressed. Here, it is crucial to note that the 2.98 eV energy difference between the ground states of Ce^{3+} and Sm^{2+} is less than the internal Ce^{3+} ($5d_1$-$^2F_{5/2}$, $^2F_{7/2}$) luminescence transitions that occur at 3.44 and 3.76 eV. Thus, a tunnelling process from the Sm to Ce ground states must be non-radiative (witnessed by the absence of any significant after-glow). Consequently, with a synchrotron pump photon alone, electron transfer between the Ce^{3+} ground state and excited states of Sm^{2+} would normally go undetected, since $(Sm^{2+})^*$ immediately relaxes to its ground state, followed by a non-radiative tunnelling process back to the cerium. As shown in figure 9, the application of the laser probe interrupts this non-radiative cycle by allowing the excitation of electrons from Sm^{2+} ground state to the conduction band; some of these electrons will be lost to the system (leaving a $[Ce^{4+}, Sm^{3+}]$ close-ion pair), becoming trapped elsewhere in the lattice (such as at isolated Sm^{3+} sites), but some will recombine at the Ce^{4+} through a radiative process as depicted in equation (4). This process can be either prompt, or via the laser-induced eviction from re-trapped charge at isolated Sm^{2+} centres. It is this process of recombination at Ce^{4+} centres that is manifested as an increase in luminescence yield on application of the laser probe; the increase is observed because the efficiency of non-resonant internal Ce^{3+} excitation is inherently low to begin with at these excitation energies. The slow rise to equilibrium (figure 5(c)) can be interpreted as the generation of Ce^{4+} through excitation of the close (Ce/Sm) ion pairs.

The laser quenching of synchrotron-pumped luminescence can also be understood from the above model, as shown in figure 10; here, strong luminescence is induced when electrons are excited to the 5d states of Ce^{3+}, whether the cerium is isolated, or in close proximity to Sm. However, in the case of the close pairs, then in the steady state some electrons will be transferred through overlapping energy states to the samarium, and these may return to cerium through the non-radiative tunnelling process. Again, without the laser probe,

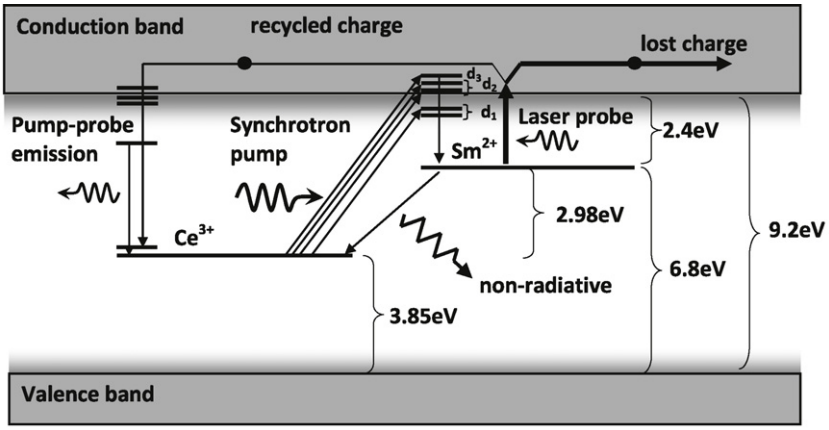

Figure 9. Full schematic energy level diagram explaining the origin of the *positive-component* pump–probe spectrum (energy levels are drawn to scale). The synchrotron pump can excite electrons from the Ce to Sm from where, once relaxed to the ground state, tunnel back to Ce; this entire process is non-radiative (at least, within the Ce^{3+} UV emission window). The application of the laser during this cycle interrupts this cycle by exciting charge from the Sm to the conduction band: some of this charge is re-trapped elsewhere in the lattice, whilst some is fed back into a radiative process; the enhanced luminescence signal thus allows selective analysis of the energy levels involved in charge transfer between the Ce and Sm.

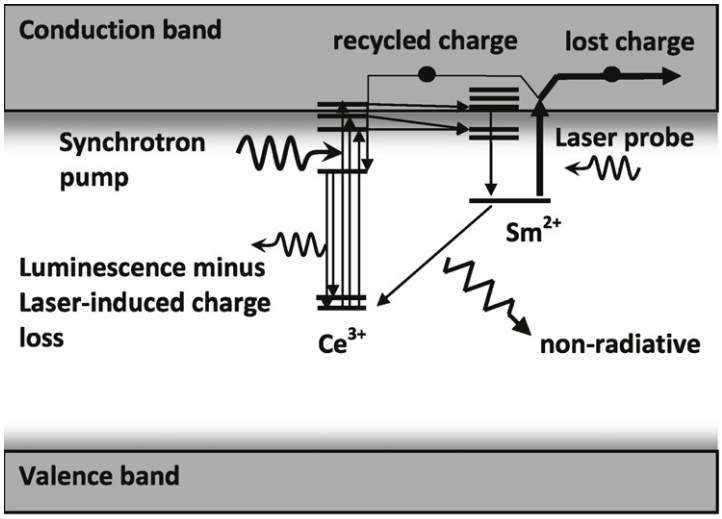

Figure 10. Full schematic energy level diagram explaining the origin of the *negative-component* pump–probe spectrum (energy levels are drawn to scale). During synchrotron stimulation of the Ce ion, via its excited states, some charge is lost to nearby Sm due to the overlap of excited state energy levels; the charge returns to the Ce via non-radiative tunnelling. In standard luminescence excitation spectroscopy, the presence of this non-radiative channel is hidden (the luminescence being an equilibrium between radiative and non-radiative processes). Application of the laser disturbs the equilibrium by evicting charge from the Sm^{2+} defects to the conduction band; if more is lost to the system (by trapping elsewhere in the lattice) than is gained by recycling, the laser will quench the Ce^{3+} emission.

this non-radiative part of the luminescence excitation process would not normally be apparent. However, as above, the laser probe will evict electrons from the Sm^{2+} ground state to the conduction band; some of these electrons will recombine radiatively at Ce (the process of equation (4)); in which case, this would lead to an enhancement of the luminescence on application of the laser probe. However, charge can also be lost to the system by re-trapping elsewhere in the lattice (such as electron capture by isolated Sm^{3+} centres), leaving the close-ion pairs in the $[Ce^{4+}, Sm^{3+}]$ charge states; Ce^{4+} can only participate in the emission being monitored by electron capture, and this is a much less efficient luminescence process than via internal excitation of Ce^{3+} to its various excited states. If this process dominates, then overall, the efficiency of Ce^{3+} luminescence is correspondingly quenched, and the rate of quenching relates to the rate of Ce^{4+} generation.

Whilst the arguments above (and models of figures 9 and 10) explain the reasons for the luminescence intensity changes and their pump energy positions, they cannot of themselves fully explain the observed dynamics of the transitions. For example, the return to equilibrium following laser quenching of the Ce^{3+} luminescence could be entirely

explained by the tunnelling process from the Sm^{2+} ground state (as depicted in figure 10) that is known to take place if this occurs at the rate observed (5 s time constant). However, the tunnelling route cannot fully explain the decay in luminescence after the laser probe is removed from the *enhancing* pump–probe interactions; why does this pump-only luminescence decay, and not simply revert immediately to the equilibrium level? One potential answer is that the synchrotron pump itself also acts to remove charge from the spatially correlated Sm^{2+} defect levels, to the conduction band. Here it is crucial to note the difference in energy between the laser and synchrotron; the laser stimulates charge to low-down in the conduction band (where preferentially, it will recombine at nearby centres), whereas the synchrotron would stimulate charge much higher in the conduction band, enabling recombination at Ce^{4+} defects further afield; the slow decay observed would then be simply the entire system reverting back to the equilibrium point.

As a final comment, the explanation of the strong synchrotron–laser excitation peaks of figures 6 and 7 inevitably requires the presence of closely correlated defect pairs for the direct transfer of charge between the defects; as a result, it may reasonably be expected that the intensity of the interactions would be dopant concentration dependent. Indeed, for the low-doped sample, the sharp resonant features (between 4.5 and 6.2 eV) are still present, but very much weaker (about 1/10 as intense; see figure 6(a)), thus partly confirming the hypothesis. It is also worth noting that this is not the case for the fast-response level difference ($\Delta_1 - \Delta_2$); this is essentially the same in both samples, and indicates that the laser is liberating electrons from Sm^{2+} that is spatially separated from Ce^{4+} (where the charge has been generated in similar fashion to that described in section 3.2).

3.3.4. Interpretation of the signals III: the role of excitons. Reference to the luminescence excitation spectra of both the Sm^{3+} and Ce^{3+} bands of figure 1 shows that exciting at the exciton absorption energy (8.2–8.7 eV) causes increases in the luminescence yield of both these *defect* centres. Consequently, although excitons are being created in the lattice, it is clear that some must transfer their energy to the defects, probably via the process shown in equation (8) below (an equivalent process is expected for the case of Sm^{3+}).

$$[Sm^{3+}, Ce^{3+}] + (e + h)_{exciton} \rightarrow [Sm^{3+}, (Ce^{3+})^*] \rightarrow [Sm^{3+}, Ce^{3+}] + h\nu \quad (8)$$

$$[Sm^{3+}, Ce^{3+}] + (e + h)_{exciton} \rightarrow [Sm^{2+}, Ce^{4+}]. \quad (9)$$

In the case where a laser probe is used in addition to the synchrotron pump, very strong interactions are observed (figures 5(d) and 6(a), (b)), quenching the Ce^{3+} emission. The dynamics of this process are indistinguishable from the pump–probe interactions involving the excited states of Ce^{3+} itself (i.e. strong quench on application of the laser, followed by slow exponential recovery to equilibrium once the probe light is removed). As these features are notably absent in the low-doped material (see figure 6(a)), it is concluded that spatially correlated Ce–Sm defects play a crucial role. As such, the spectral features suggest that the charge cycling processes follows equation (9), instead; following the electron transfer via the Ce^{3+} excited states, the interaction of the laser would be as given in figure 10.

3.4. Energy level scheme within the model framework

The results of this work places the divalent Sm ground state relative to the valence band at 6.9 eV (from the position of the charge transfer band in figure 1) or at 6.8 eV (the energy of the Sm OSL-creation band in figure 3). The Ce^{3+} ground state has been placed at 5.3 eV below the conduction band based on the OSL-creation resonance in figure 3 (tentatively assigned to excitation of an electron from the ground state of Ce to the conduction band edge). From the high energy photo-creation of OSL, the bandgap energy E_{VC} has been determined to be 9.2 eV. Within this scheme, the resulting energy difference of 2.9 eV between the ground states of Ce^{3+} and Sm^{2+} appear fully consistent with the value of 2.98 eV derived from the two-photon spectroscopy results in figure 8(b), wherein it was proposed that direct transitions between the two defects are possible.

We are now in a position to be able to compare these energy levels with those of *all* the lanthanides in YPO_4, both trivalent and divalent, relative to the band edges. Using the method outlined in Dorenbos (2003) and Dorenbos (2005b) and the parameter set from Dorenbos *et al* (2010), the scheme of figure 11 is made. The levels in blue colour belong to the trivalent lanthanides and those in red to the divalent ones. The 4f ground state energies belonging to the trivalent lanthanides have been connected by a solid line, which reproduces the familiar double zigzag curve; the same has been done for the divalent lanthanides. The $4f–5d_1$ energy difference for Ce^{3+} in YPO_4 defines the so-called red-shift parameter, which enables us to estimate the corresponding energy differences for each other trivalent lanthanide. It also enables us to predict the 4f to lowest 5d state energy difference for each divalent lanthanide ion. These predictions give us the location of the lowest 5d state for all trivalent and divalent lanthanides as drawn in figure 11. The lowest energy Sm^{3+} 4f–5d transitions near 7.1 eV in figure 1(b) agrees with the predictions from the scheme in figure 11. Also the energy of the lowest 5d band (the A-band at 1.7 eV and B-band at 1.9 eV) of Sm^{2+} from figure 8(a) agrees with the prediction from figure 11. For Ce^{3+} we have drawn the location of all five 5d states from figure 1(a) in the scheme. Note that the $5d_4$ and $5d_5$ states are inside the conduction band. For Sm^{2+} we have drawn the location of the A and B levels of the $5d_1$ and $5d_2$ states from figure 8(b) in figure 11, the latter being inside the conduction band. Note that one can project all the levels and transitions depicted in figures 1, 4, 9 and 10 in the scheme of figure 11.

Figure 11 is also fully in accord with other information we have to locate lanthanide energy levels. The energy of charge transfer to, for example, Eu^{3+}, Yb^{3+}, Tm^{3+}, Dy^{3+}, Er^{3+} are well established and they all correspond with the energy difference between the valence band and the ground state location of the respective divalent lanthanides in figure 11. In Bos *et al* (2008) we have demonstrated that the scheme is consistent with thermoluminescence data that

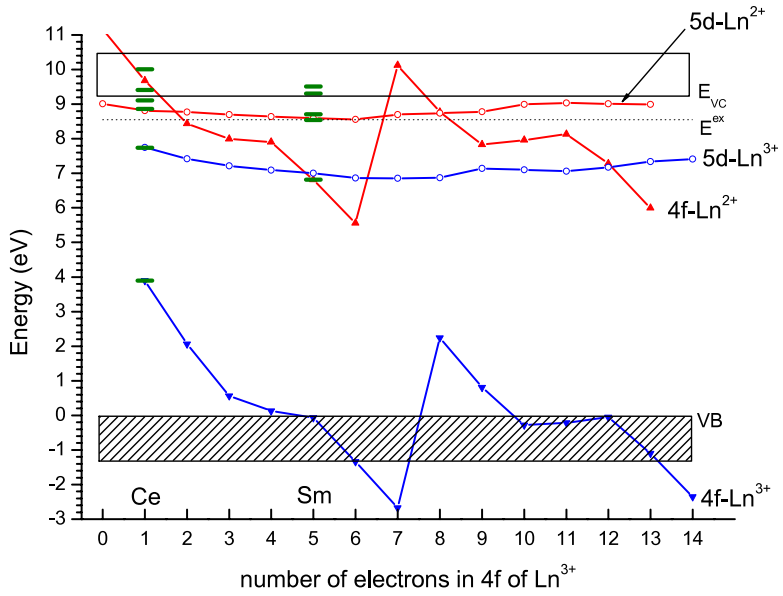

Figure 11. Energy level diagram for YPO_4 showing the location of the 4f and 5d states of divalent (red) and trivalent (blue) lanthanides, following the most recent parameters published in Dorenbos *et al* (2010). The absolute positions of the ground and excited states of Ce^{3+} and Sm^{2+}, as derived from the present work, are depicted by the green bars.

probes the location of the divalent ground state energy below the conduction band.

The great value of figure 11 is that we now can select other combinations of trivalent lanthanides and predict the outcome of the type of pump and probe experiments reported in this work. The model to place the lanthanide levels in compounds has developed on a piecemeal basis since around 2002 (e.g. Thiel *et al* 2002, Dorenbos 2003) and is continually being verified and improved and, when needed, a new parameter set is proposed to better construct those schemes (e.g. Dorenbos *et al* 2010). With the pump and probe experiments on other lanthanide pairs in both YPO_4 and other compounds we intend to further verify and further refine those parameter sets.

4. Conclusions

In this work, we have demonstrated that the additional use of a laser probe, deployed whilst undertaking luminescence excitation spectroscopy on compounds co-doped with electron and hole trapping centres, can provide a wealth of information regarding interactions between the defects that would not be readily accessible by other means—particularly those involving non-radiative charge transfer routes. In the specific case of YPO_4:Ce, Sm studied here, the work has not only provided a detailed analysis of such interactions in this material (including the first report of direct excitation from cerium to samarium ions which do not involve mediation by the conduction band), but it has also allowed the bandgap energy to be determined accurately for the first time, together with a precise positioning of the defect levels within the bandgap; the latter are in excellent correspondence with the model predictions. The experimental approach promises a step-change in the way such materials can be studied in the future, and will help in tailoring the properties of luminescent materials.

Acknowledgments

The authors would like to thank Drs A Bessière and A Lecointre of the Ecole National Supérieure de Chimie de Paris for the synthesis of the samples used in this study. The work is funded by in the UK by EPSRC grant EP/F065272/1, and in The Netherlands by Delft University of Technology (TUD grant TTQ700). We are grateful for beamtime awards at STFC Daresbury Synchrotron Radiation Source, references 50028 and 50053.

References

Bos A J J, Dorenbos P, Bessière A and Viana B 2008 Lanthanide energy levels in YPO_4 *Radiat. Meas.* **43** 222–6

Bos A J J, Poolton N R J, Wallinga J, Bessière A and Dorenbos P 2010 Energy levels in YPO_4:Ce^{3+}, Sm^{3+} studied by thermally and optically stimulated luminescence *Radiat. Meas.* at press (doi:10.1016/j.radmeas.2010.01.014)

Chakrabarti K, Mathur V K, Thomas L A and Abbundi R J 1989 Charge trapping and mechanism of stimulated luminescence in CaS:Ce, Sm *J. Appl. Phys.* **65** 2021–3

Dorenbos P 2003 Systematic behaviour in trivalent lanthanide charge transfer energies *J. Phys.: Condens. Matter* **15** 8417–34

Dorenbos P 2005a Mechanism of persistent luminescence in Eu^{2+} and Dy^{3+} codoped aluminate and silicate compounds *J. Electrochem. Soc.* **152** H107–10

Dorenbos P 2005b The Eu^{3+} charge transfer energy and the relation with the band gap of compounds *J. Lumin.* **111** 89–104

Dorenbos P and Bos A J J 2008 Lanthanide level location and related thermoluminescence phenomena *Radiat. Meas.* **43** 139–45

Dorenbos P, Krumpel A H, van der Kolk E, Boutinaud P, Bettinelli M and Cavalli E 2010 Lanthanide level location in transition metal complex compounds *Opt. Mater.* at press (doi:10.1016/j.optmat.2010.02.021)

Huntley D J and Lamothe M 2001 Ubiquity of anomalous fading in K-feldspars and the measurement and correction for it in optical dating *Can. J. Earth Sci.* **38** 1093–106

Karanjikar N P and Naik R C 1988 X-ray excited optical luminescence of Ce^{3+} in YPO_4 and location of 5d levels *Solid State Commun.* **65** 1419–22

Keller S P and Pettit G D 1958 Quenching, stimulation, and exhaustion studies on some infrared stimulable phosphors *Phys. Rev.* **111** 1533–9

Krumpel A H, Bos A J J, Bessière A, van der Kolk E and Dorenbos P 2009 Controlled electron and hole trapping in YPO_4:Ce^{3+}, Ln^{3+} and $LuPO_4$:Ce^{3+}, Ln^{3+} (Ln = Sm, By, Ho, Er, Tm) *Phys. Rev.* **80** 085103

Lakshmanan A R 1999 Photoluminescence and thermostimulated luminescence processes in rare-earth doped $CaSO_4$ phosphors *Prog. Mater. Sci.* **44** 1–187

Mathur V K, Gasiot J, Abbundi R J and Brown M D 1986 Optically stimulated luminescence in MgS:Ce, Sm *Radiat. Prot. Dosim.* **17** 333–6

Meijerink A, Schipper W J and Blasse G 1991 Photostimulated luminescence and thermally stimulated luminescence of Y_2SiO_5:Ce, Sm *J. Phys. D: Appl. Phys.* **24** 997–1002

Poolton N R J, Hamilton B and Evans D A 2005 Synchrotron–laser pump–probe luminescence spectroscopy: correlation of electronic defect states with x-ray absorption in wide-gap solids *J. Phys. D: Appl. Phys.* **38** 1478–84

Poolton N R J, Towlson B M, Evans D A and Hamilton B 2006 Synchrotron–laser interactions in hexagonal boron nitride: an examination of charge trapping dynamics at the boron K-edge *New J. Phys.* **8** 76

Quinn F, Poolton N, Malins A, Pantos E, Andersen C, Denby P, Dhanak V and Miller G 2003 The mobile luminescence end-station, MoLES: a new public facility at Daresbury synchrotron *J. Synchrotron Radiat.* **10** 461–6

Sidorenko A V, Dorenbos P, Bos A J J, van Eijk C W E and Rodnyi P A 2006 Lanthanide level location and charge carrier trapping in $LiLnSiO_4$:Ce^{3+}, Sm^{3+}, Ln = Y or Lu *J. Phys.: Condens. Matter* **18** 4503–14

Thiel C W, Sun Y and Cone R L 2002 Progress in relating rare-earth ion 4f and 5d energy levels to host bands in optical materials for hole burning, quantum information and phosphors *J. Mod. Opt.* **49** 2399–411

van Pieterson L, Reid M F, Wegh R T, Soverna S and Maijerink A 2002 $4f^n \rightarrow 4f^{n-1}$ 5d transitions of the light lanthanides: experiment and theory *Phys. Rev.* B **65** 045113